Accepted Manuscript

Title: Uphill filling system for a bar-like casting

Author: Lintao Zhang Kenny W.Q. Low Fawzi Belblidia
Johann Sienz

PII: S0924-0136(18)30283-8
DOI: https://doi.org/doi:10.1016/j.jmatprotec.2018.06.036
Reference: PROTEC 15820

To appear in: *Journal of Materials Processing Technology*

Received date: 27-10-2017
Revised date: 22-6-2018
Accepted date: 23-6-2018

Please cite this article as: Lintao Zhang, Kenny W.Q. Low, Fawzi Belblidia, Johann Sienz, Uphill filling system for a bar-like casting, *<![CDATA[Journal of Materials Processing Tech.]]>* (2018), https://doi.org/10.1016/j.jmatprotec.2018.06.036

Uphill filling system for a bar-like casting

Lintao Zhang*, Kenny W. Q. Low, Fawzi Belblidia, Johann Sienz

Advanced Sustainable Manufacturing Technologies (ASTUTE 2020), College of Engineering, Swansea University, Bay Campus, Fabian Way, Swansea SA1 8EN, UK

Abstract

Bar-like sand mould tilted angle reduced free surface fluctuations. The primary and secondary reflected wave heights decreased with the scaling of $Re^{0.8}$ and $Re^{0.55}$, respectively. These heights were reduced by 54% and 51% when θ was increased from 0° to 5°. A larger tilted angle was found to generate an air cavity in the cast, the size of which was observed to vary with Reynolds number (Re). An optimised range of tilted angle (2° to 3°) was proposed as a compromise to reduce the free surface fluctuations and maintain a perfect casting shape at the end of the filling stage.

Keywords: Sand casting, Filling behaviour, Mould design, Computational Fluid Dynamics, Co-Cr-W alloy

1. Introduction

The sand casting process consists of two main stages: (i) the filling stage, and (ii) the solidification stage. Although the filling stage has a much shorter time scale than the solidification stage, it plays a crucial role in determining the quality of the cast. Therefore, it is essential to have a better understanding of the fundamental flow dynamics of the filling phase.

The cavity is enclosed during production, making it difficult to visualise the filling pattern and anticipate the cast quality. Advanced computational modelling techniques have become an attractive tool to provide qualitative and

*Corresponding author
URL: L.Zhang@swansea.ac.uk (Lintao Zhang)

quantitative predictions on the underlying filling phenomena. Furthermore, a reliable computational strategy is required to capture the behaviour of the free metal surface throughout the filling process. Different numerical schemes and algorithms have been developed over recent decades. Ramshaw et al. (1976) presented a numerical method for calculating single-component two-phase fluid flow, for both a fixed and a moving interface, at low Mach numbers. This method was successfully applied to one-dimensional oscillations in the water level in a vertical pipe and two-dimensional water sloshing behaviour. However, in three-dimensional cases, this method required the interface data to be preserved, which made computation expensive. Hirt & Nichols (1981) further explored the Volume of Fluid (VoF) method to deal with complicated free boundary conditions. This method was particularly powerful because minimum storage information was required and the intersecting free boundaries were treated automatically. Chan et al. (1991) described a three-dimensional model to simulate the filling process of molten alloy in sand casting. The model was based on a conserved scalar variable and it used an adaptation of the van Leer scheme in order to capture the metal-air interface. The numerical results obtained were validated against a water model die-casting experiment. However, this method was computationally expensive for the highly irregular element types. Ravindran & Lewis (1998) presented a finite element algorithm to simulate mould filling process. The Navier-Stokes equations were solved by using the Galerkin finite element method and the metal-air front was tracked using a pseudo-concentration approach. Kim et al. (2006) developed an adaptive refinement technique based on tetrahedral and hexahedral grids where refined elements were employed in the vicinity of the metal-air interface and coarse elements were applied elsewhere to maintain a similar numerical cost. The method was validated against a benchmark configuration. Pang et al. (2010) presented a novel approach, known as the SOLA particle level set method, to deal with the sharp interface configuration in the mould filling process. This method was validated using a water model experiment. Mirbagheri et al. (2003) developed a code that included heat transfer and permeability of coating using a finite

difference method based on SOLA-VOF method. The results obtained from the SOLA-VOF approach were validated against a designed aluminium alloy filling experiment in a transparent mould.

With these powerful numerical techniques being developed, research on the filling stage can be performed in order to better understand the filling dynamics and to optimise the sand mould configuration, hence enhancing the product quality and reducing the energy consumption. For instance, Zhang et al. (2017) reduced the wastage of Ni-Co-W alloy in the riser by optimising the gates' location using a filling simulation. Sun et al. (2008) investigated the relationship between the gating system dimensions and the quality, e.g. the shrinkage porosity, of a magnesium casting. They concluded that the runner height was the most significant factor influencing the casting quality. Kermanpur et al. (2008) studied filling and solidification behaviour of the molten alloy, and the factors of the surface roughness and the contact angles were also taken into account. This filling simulation suggested an optimised gate cross-section dimension could be optimised to avoid air absorption affecting the casting quality. Du et al. (2015) optimised the process parameter for an enclosed gating system and a complete casting without any defect. Assar (1999) conducted experiments and correlated the mass flow rate of the filling with the microstructure of the casting (Al-4.5Cu ingots). In his experiment, coarser equiaxed grains and short columnar grains were obtained at high values of mass flow rate. Cox et al. (2000) investigated the influence of top and bottom filling on the mechanical performance of Al, Fe and Ni based alloy. They found that for Al based alloy, bottom filling was a better choice than top filling. This short literature review demonstrates that the VoF technique is a well-established numerical method to capture metal-air interface variation. It will be adopted in the current work.

The quality of casting is primarily influenced by the occurrence of free surface fluctuations (Campbell, 1991). Liu et al. (2015) investigated the influence of pressurising speed on the mechanical properties of Al based alloy casting. The results showed high molten metal velocity could result in oxide film entrapment. This was due to the flow surface fluctuation, e.g. the resultant relative rotating

vortex. Campbell (1991) stated that these flow free surface fluctuations could cause air entrapment and generate flaws. One of the techniques to reduce free surface fluctuation is to adopt an uphill filling system, especially for large scale flat plate-like castings. Carswell et al. (2011) adopted this method for small scale ($\sim$ 0.1 m) disc-like castings to improve quality. Despite some success in enhancing the cast quality in disc-like castings, the uphill filling system has not been examined on a bar-like castings, heavily influenced by its bounded wall effects. In contrast, the disc-like uphill filling system is mainly adopted to suppress 'mis-run' of the molten flow front. However, the system on a bar-like cast is susceptible to produce air void for large filling angles. This could cause the cast configuration to be incomplete, leading to parts being recycled.

In this present work, the bar-like sand casting process for Co-Cr-W alloy is conducted through numerical simulations with aims:

1. to a better understanding of the flow behaviour of this type of filling system;
2. to identify a suitable configuration for the uphill filling system that produces good quality cast.

The outline of the present paper was as follows. In Section 2, the mould configuration and material properties of the alloy adopted in this work were explained. The governing equations and numerical procedures for the filling process were described. In Section 3, the results obtained from the simulations were analysed and findings relating to the aims were presented. The main conclusions were summarised in Section 4.

2. Configuration and numerical set-up

2.1. Mould configuration and material properties

The cast configuration, originated from a local company sand's mould design, was depicted in Fig. 1. Owing to the symmetrical nature of the configuration, only half of the whole mould was presented. Different mould parts were labelled

accordingly. The origin O was located in the middle of the casting bar cavity front wall. For the coordinates, $x-$ and $y-$axes were defined as radial directions and $z-$axis was defined along the axial direction of the casting bar. The tilted angle, θ, was defined as the angle between the casting bar cavity (axis direction) and the ground, as shown in the figure.

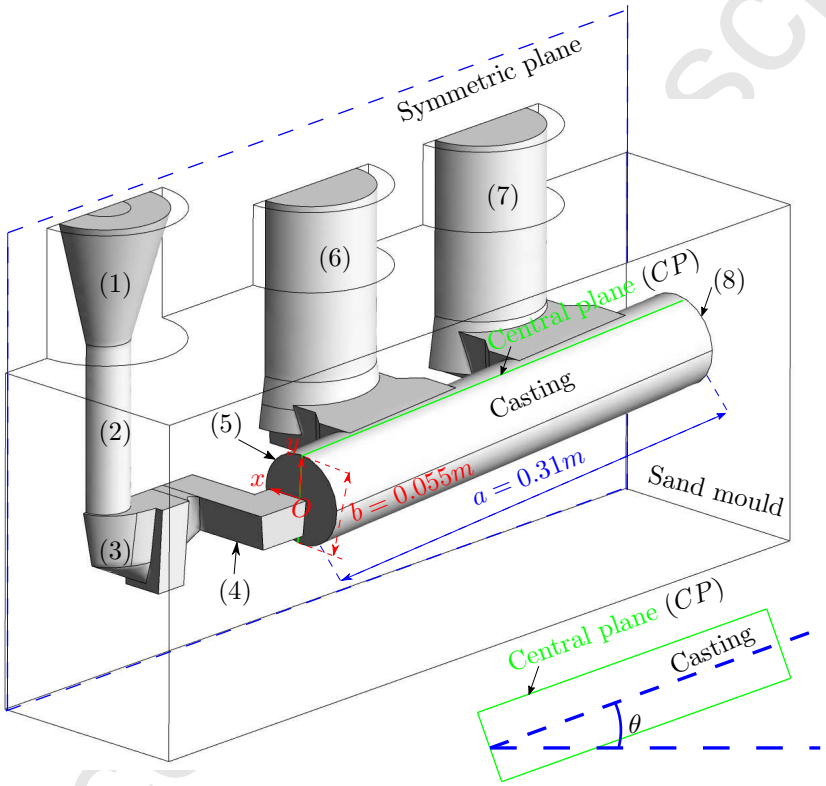

Figure 1: Sand mould configuration. (1): the pouring basin, (2): the sprue, (3): the choke, (4): the runner bar, (5): front wall of casting, (6): the front riser, (7): the rear riser and (8): end wall of casting. θ is the tilted angle of the casting. The central plane (CP, thereafter) is defined as the $y-z$ plane at $x=0$.

The chemical properties of the Co-Cr-W alloy were tabulated in Table 1. For molten alloy, the density and dynamic viscosity were taken to be 8.3 $\times 10^3$ kg m^{-3} and 4 $\times 10^{-3}$ kg m^{-1} s^{-1}, respectively (Zhang et al., 2017). The specific heat c_p and thermal conductivity σ were calculated based on the Kopp-Neumann

rule of mixtures (Valenci and Quested, 2008):

$$c_p = \sum_{i=1}^{n} (c_{pi} \cdot X_i), \tag{1}$$

and

$$\sigma = \sum_{i=1}^{n} (\sigma_i \cdot X_i), \tag{2}$$

where c_{pi} and σ_i were the specific heat and the thermal conductivity of the pure component i, respectively. X_i was the weight percentage of i composition. As the filling time is short, the material properties were assumed to be temperature independent. The specific heat and thermal conductivity the alloy (sand) are 533.8 (990) J kg^{-1} K^{-1} and 36.5 (0.75) W m^{-1} K^{-1}, respectively.

Table 1: Chemical compositions for Co-Cr-W alloy (in wt.%).

Element	C	Cr	W	Ni	Fe	Si	Co
Composition	0.8	30	14	< 3	< 3	1.5	Bal.

2.2. Governing equations and numerical set-up

The filling behaviour of the molten alloy was investigated by adopting the homogeneous free surface model and the heat transfer features were studied by solving the energy equation using CFX solver.

2.2.1. Governing equations for fluid domain: molten alloy

During the filling process, two phase flow were involved: (i) the liquid alloy ('L') phase and (ii) the air ('A') phase. The homogeneous free surface model was found to be an effective method for simulating the filling process where the phases were stratified (immiscible) with a well defined interface between them. The proposed model involved various physics phenomena, including multiphase flow, gravitational force, surface tension, temperature and flow kinematics. The general form of the continuity, momentum and energy equations can be written as follows, respectively:

$$\frac{\partial \rho}{\partial t} + \boldsymbol{\nabla} \cdot (\rho \mathbf{u}) = 0, \tag{3}$$

$$\frac{\partial \mathbf{u}}{\partial t} + \boldsymbol{\nabla} \cdot (\mathbf{u} \otimes \mathbf{u}) = -\frac{\boldsymbol{\nabla} p}{\rho} + \nu \boldsymbol{\nabla}^{\mathbf{2}} \mathbf{u} + \mathbf{f}, \tag{4}$$

and

$$\rho \frac{\partial e}{\partial t} + \boldsymbol{\nabla} \cdot (\rho e \mathbf{u}) = \boldsymbol{\nabla} \cdot \sigma \boldsymbol{\nabla} T + \mathbf{S}_E. \tag{5}$$

where ρ, t, $\mathbf{u}$, p, ν, $\mathbf{f}$, e, T and $\mathbf{S}_E$ denoted the density, time, velocity, pressure, kinematic viscosity, gravitational force, energy, temperature and heat source term, respectively. By using the homogeneous free surface multiphase model, the Eq. 3 can be written as:

$$\frac{\partial}{\partial t}(\rho^{cv}) + \boldsymbol{\nabla} \cdot (\rho^{cv} \mathbf{u}^{cv}) = 0, \tag{6}$$

where the density ρ^{cv} and the velocity $\mathbf{u}^{cv}$ in the control volume can be calculated as:

$$\rho^{cv} = \rho_L \gamma_L + \rho_A \gamma_A, \tag{7}$$

and

$$\mathbf{u}^{cv} = \frac{\rho_L \gamma_L \mathbf{u}_L + \rho_A \gamma_A \mathbf{u}_A}{\rho^{cv}}. \tag{8}$$

In Eq. 7 and Eq. 8, ρ_L, γ_L, $\mathbf{u}_L$, ρ_A, γ_A and $\mathbf{u}_A$ were the density, the volume fraction and the velocity for 'L'-phase and 'A'-phase, respectively. In terms of volume fraction, for a single cell:

$$\gamma_L = \begin{cases} 0 & \textit{empty of 'L'-phase}, \\ 0 < \gamma_L < 1 & \textit{mixture of 'L'-phase and 'A'-phase}, \\ 1 & \textit{full of 'L'-phase}, \end{cases} \tag{9}$$

Clearly, for a two phase problem, the equation of the conservation of volume fraction for a single cell gave:

$$\gamma_A + \gamma_L = 1, \tag{10}$$

and

$$\frac{\partial (\gamma_L \rho_L)}{\partial t} + \boldsymbol{\nabla} \cdot (\gamma_L \rho_L \mathbf{u}^{cv}) = 0. \tag{11}$$

For Eq. 4, it can be written as

$$\frac{\partial}{\partial t}(\rho^{cv} \mathbf{u}^{cv}) + \boldsymbol{\nabla} \cdot (\rho^{cv} \mathbf{u}^{cv} \otimes \mathbf{u}^{cv} - \mu^{cv} (\boldsymbol{\nabla} \mathbf{u}^{cv})) = -\boldsymbol{\nabla} p + \mathbf{S}_M, \tag{12}$$

where μ^{cv} was the dynamic viscosity:

$$\mu^{cv} = \mu_L \gamma_L + \mu_A \gamma_A. \tag{13}$$

In Eq. 12, $\mathbf{S}_M$ was the momentum source term, which accounted for the surface tension and gravity. For surface tension, the continuum surface force (CSF) model (Brackbill et al., 1991) was adopted:

$$\mathbf{S}_M = \rho_L \mathbf{g} + \sigma_s \kappa \boldsymbol{\nabla}_\alpha, \tag{14}$$

where σ_s, κ and $\boldsymbol{\nabla}_\alpha$ were the surface tension coefficient, the curvature of the interface and the normal direction of the interface, respectively. Furthermore, neglecting the source term, the total energy equation can be written as:

$$\frac{\partial(\rho^{cv} h_{tot})}{\partial t} - \frac{\partial p}{\partial t} + \boldsymbol{\nabla} \cdot (\rho^{cv} \mathbf{u} h_{tot}) = \boldsymbol{\nabla} \cdot (\sigma_{eff} \boldsymbol{\nabla} T) + \boldsymbol{\nabla} \cdot (\mathbf{u} \cdot \boldsymbol{\tau}), \tag{15}$$

where h_{tot} was the total enthalpy:

$$h_{tot} = h + \frac{1}{2}\left(|\mathbf{u}^{cv}|^2\right), \tag{16}$$

and

$$\sigma_{eff} = \gamma_L \sigma_L + \gamma_A \sigma_A, \tag{17}$$

where σ_L and σ_A were the thermal conductivity of the 'L' and 'A' phases. The σ_{eff} was the effective thermal conductivity. The proposed computational model for the liquid domain consisted of five variables defined over five governing equations.

2.2.2. Governing equations for the solid domain: sand

The solid domain was considered as a thermal barrier for the flow cavity where heat transfer in the sand domain ('S') was simulated through the conduction equation:

$$\frac{\partial(\rho_S h)}{\partial t} + \boldsymbol{\nabla} \cdot (\rho_S \mathbf{u}_S h) = \boldsymbol{\nabla} \cdot (\sigma_S \boldsymbol{\nabla} T) + \mathbf{S}_E, \tag{18}$$

where ρ_S, h, $\mathbf{u}_S$ and σ_S were the sand density, the enthalpy ($=\int_{T_{ref}}^{T} c_{p,S} dT$), the sand mould moving velocity and the thermal conductivity of the sand, respectively. For the current case, Eq. 18 was simplified:

$$\frac{\partial(\rho_S h)}{\partial t} = \boldsymbol{\nabla} \cdot (\sigma_S \boldsymbol{\nabla} T). \tag{19}$$

2.2.3. Boundary conditions

Symmetry boundary was imposed at the split plane (see Fig. 1) where the normal velocity component, its gradient ($\partial_x v$ and $\partial_x w$) and the temperature gradient ($\partial_x T$) were nullified. A mass flow rate of 1.48 kg s^{-1} with a pouring temperature of 1893.75 K was prescribed at the top surface of the sprue. The mass flow rate was obtained by the weight of the casting and the filling time of 10 seconds. An opening boundary condition ($\partial_n p = 0$ kg $s^{-2}m^{-1}$) was adopted for the top of both front and rear risers. The opening temperature was set to 293.15 K. No slip boundary condition was imposed at the surface between the cast and sand. A heat transfer coefficient of 6.8 W m^{-2} K^{-1} was adopted (Stefanescu et al., 1990) at the outer surface of the sand and the temperature was set to 293.15 K.

2.2.4. Solution procedure

A vertex-centered finite volume technique was used to solve the system of equations. The solver adopted a coupled pressure-based solution algorithm with a second-order high resolution spatial discretisation scheme and a second-order fully implicit temporal discretisation scheme. Furthermore, a compressive discretisation scheme for both space and time was used to ensure sharp interface of the free surface. Within each time step, an iterative scheme, known as the coefficient loop, was adopted to ensure that the linearised system of discrete equations were converged. The normalised imbalances in the system were monitored to ensure that they converge to a Root Mean Square (RMS) residual target of 1×10^{-4}. The simulation started off with a small enough time step size ($\Delta t = 5\times10^{-4}$ s) to maintain the stability (e.g. CFL requirement). The time step size was increased when the casting cavity was half filled to speed up the simulation while maintaining its stability until the cavity was filled up. Simulations were performed using the High Performance Computing Cluster at the College of Engineering at Swansea University. The cluster consists of 72 computing nodes. Each node has two Intel E5-2680 v4 Xeon processors and access to 64 GB DDR4 RAM. Furthermore, each processor has 14 cores operating

at a clock frequency of 2.4GHz with 35MB SmartCache. Each simulation was performed using 28 cores.

2.2.5. Mesh sensitivity test

A first test was performed to determine the computational grid considered for the sand mould cavity had minimal impact on the free-surface results (γ_L=0.5). Four mesh levels were proposed (M1 to M4) with the number of elements being 128,484; 931,965; 7,103,433 and 56,643,155 respectively. Fig. 2 showed the boundary profile (half) on $y-z$ plane where $x=-0.075$ m for the different meshes. Results showed that the curve became closer with an increasing number

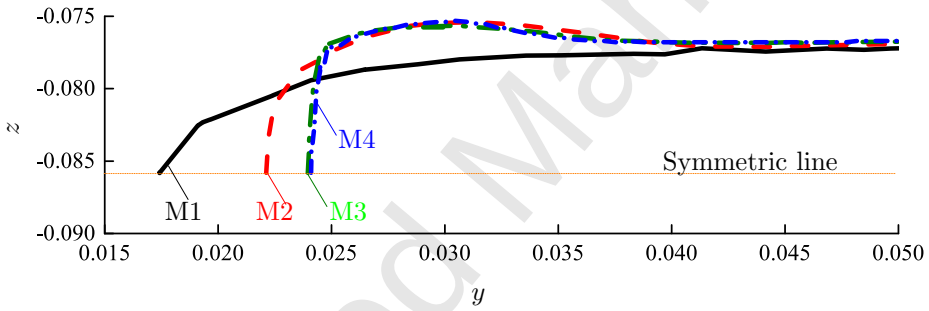

Figure 2: Iso-surface boundary profiles of γ_L=0.5 at x=-0.075 m for M1 (black), M2 (red), M3 (green) and M4 (blue), respectively.

of elements, with a good match between M3 and a more refined M4. Therefore, all simulations were based on M3, which ensured good precision at a reasonable computing cost. The mesh details of M3 was illustrated in Fig. 3. Inflation layers were imposed in the vicinity of the interface between the sand and the casting.

2.2.6. Validation experiment

An experiment was conducted to further validate the numerical simulation. The aim was to capture the sand temperature evolution with filling time at different locations in the sand mould. The temperature monitoring locations were shown in Fig. 4. Temperatures were captured using NiCr-NiSi type thermocouples and the data were saved in the data-collecting system. The distance

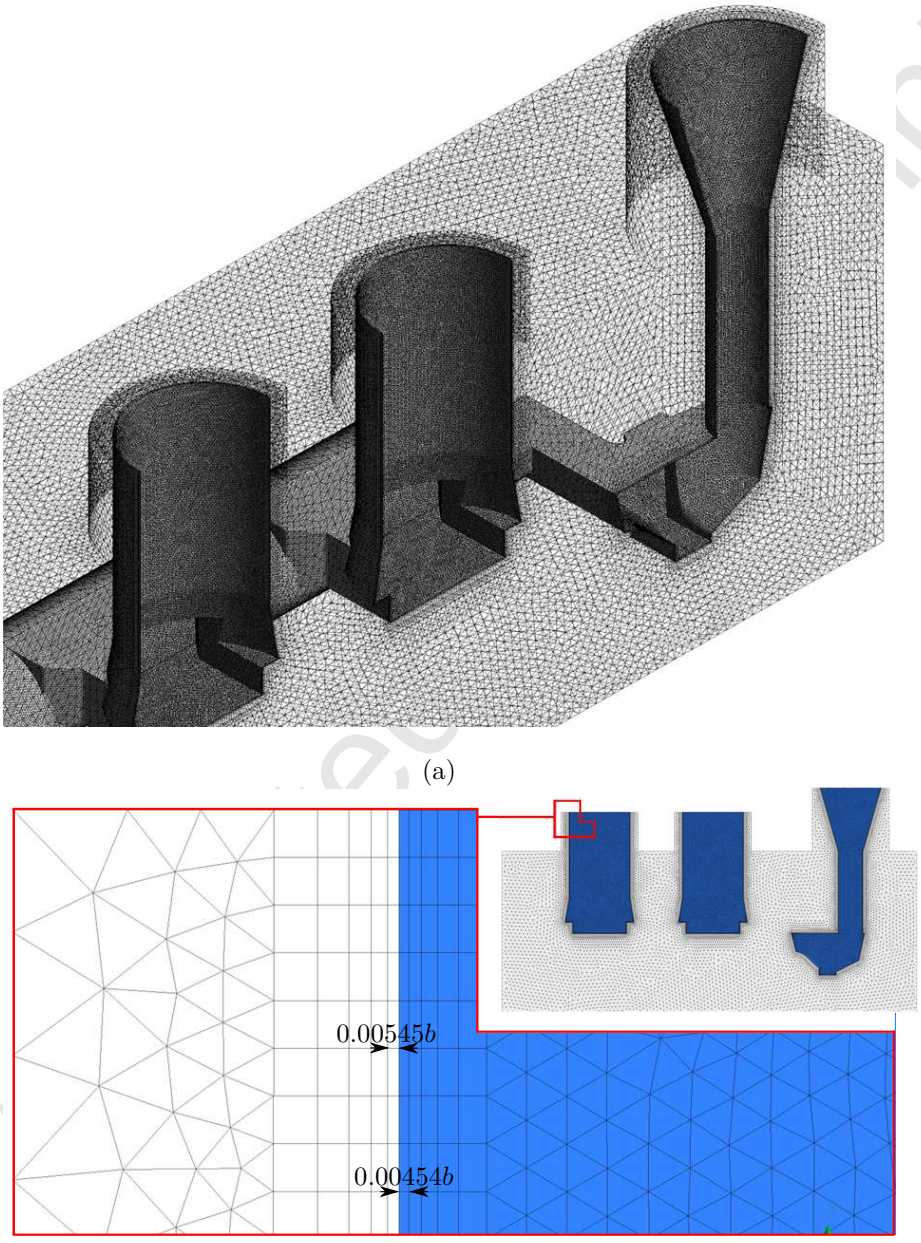

Figure 3: The detailed mesh. (a): 3D view and (b) x-axis view. For (b), the blue color stands for the cavity zone. Inflation layers were adopted in vicinity of the alloy-sand interfaces.

(a) Before filling (b) After filling

Figure 4: Experiment set-up. Sand temperatures are obtained using thermocouples and the results are used to validate the numerical set-up.

between the top of the sand mould and the tip of the thermocouples (1 to 6) was 64 mm. The pouring temperature of the alloy was 1893.15 K and the total filling time was 12 s. Results comparison between experiment (E) and simulation (S) for thermocouple 6 from filling time $t = 1$ s to 10 s were tabulated in Table 2. Furthermore, the results comparison between the experiment and

Table 2: The results of the experiment (E in the table) and simulation (S in the table) for thermal couple 6 for $t = 1$ s to 10 s. ϵ^T refers to the difference between experimental and numerical simulation. All temperature values were expressed in °C.

	filling time t, s									
	1	2	3	4	5	6	7	8	9	10
E	20.0	20.0	20.0	20.1	20.3	20.8	21.4	22.4	24.2	27.0
S	20.0	20.0	20.0	20.0	20.1	20.2	20.6	21.3	23.6	26.7
ϵ^T	0	0	0	4.97×10^{-3}	9.85×10^{-3}	2.88×10^{-2}	3.74×10^{-2}	4.91×10^{-2}	2.48×10^{-2}	1.11×10^{-2}

the simulation for thermocouple 1 to 6 at $t = 10$ s were tabulated in Table 3. It can be seen that the temperature at locations 1 to 5 were approximately 20 °C. The temperature loss was observed to be small when the filling process was completed. However, a clear temperature increase was observed at location 6 as this location was close to the sprue region. The results showed that the temper-

Table 3: The results of the experiment (E in the table) and simulation S in the table) for thermocouples 1 to 6 at $t = 10$ s. All temperature values were expressed in °C.

	monitoring locations					
	1	2	3	4	5	6
E	20.04	20.02	20.01	20.04	20.04	26.95
S	20.03	20.05	20.05	20.02	20.03	26.68
ϵ^T	4.99×10^{-4}	1.50×10^{-3}	2.00×10^{-3}	4.99×10^{-4}	4.99×10^{-4}	1.00×10^{-2}

ature discrepancies were less than 3%; hence, the proposed numerical approach was considered to be validated.

3. Results and discussion

Following the completion of mesh sensitivity and validation, the investigation on the filling behaviour in an uphill filling system of a bar-like cast was performed and an optimised configuration system was established. Two control parameters were selected: (i) the Reynolds number, Re, and (ii) tilted angle of the cast, θ. The computation of Re involved utilising the averaged inlet velocity at the front wall of casting, labelled as (5) in Fig. 1 and the height of inlet at the front wall of casting as the characteristic length. Re contributed to the internal cast quality. This was primarily associated with the beginning of the filling stage, where the reflected wave from the alloy could potentially cause free surface fluctuation. θ contributed to the external cast quality and was associated to the end of the filling stage, contributing to the occurrence of air void in the system. Analysis was carried out and discussions were presented in terms of the two aforementioned aspects which were the reflect waves and break-up along with the occurrence of air void. A total of four Re values (8,350, 16,700, 25,050 and 33,400) and six θ values (0° to 5°) were adopted.

3.1. Reflected waves and break-up

The molten alloy initially followed the path from the pouring basin, sprue, choke and runner bar. Once having entered the front wall into the casting cavity

at a particular tilted angle, it would tend to travel along the length of the casting cavity towards the end wall. The effect of gravity became more pronounced with increasing tilted angle, and the molten alloy started to accumulate in the vicinity of the front wall. Furthermore, the increase in Re helped to overcome the gravitational force and arrived at the end wall using a shorter time.

The evolution of the reflected wave for $Re = 16,700$ and $\theta = 0°$ was illustrated in Fig. 5. The filling time t was normalised using the averaged velocity and the diameter of the bar cavity b, forming a normalised filling time t^*. As the

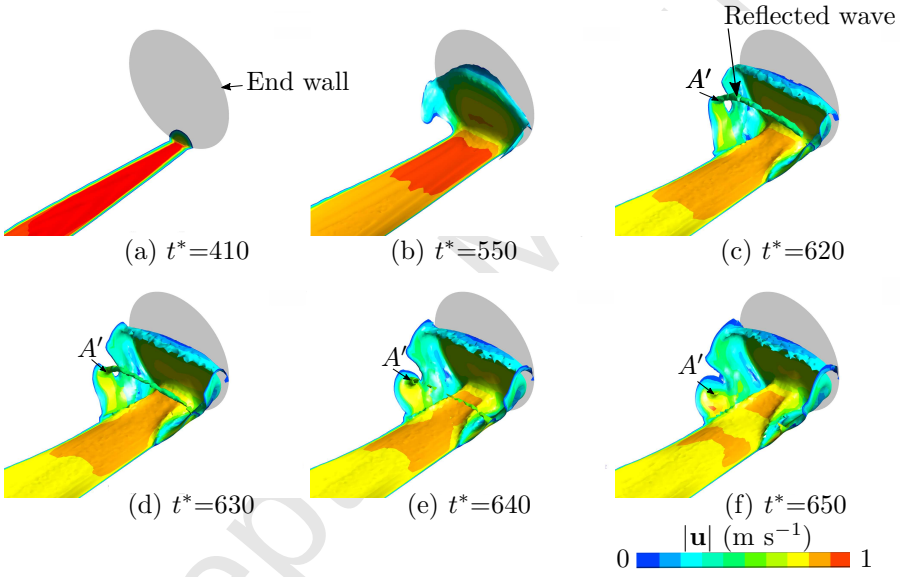

Figure 5: Velocity magnitude ($|\mathbf{u}|$) distribution at different normalised filling time t^* overlaid on iso-surface of $\gamma_L = 0.5$ at Re=16,700. The primary reflected wave is presented.

molten alloy reached the end wall, depicted in Fig. 5 (a), it was then forced to travel up along the $x-$ and $y-$ directions, attaching to the end wall as depicted in Fig. 5 (b). The molten flow front continued to raise along the end wall to a certain maximum height, where an interesting phenomenon, known as the "reflected wave break-up" was captured. The wave boundary A' was subsequently seen to be moving downwards. This phenomenon was mainly caused by the intensity of incoming molten velocity initiated by the tilted angle θ. This was observed clearly in Fig. 5 (c) to (f). A similar type of phenomenon (for larger

tilted angle values: e.g. 30°) was observed in the work of Xie et al. (2017). The molten flow front was observed to be travelling at a much higher speed when the configuration was flat ($\theta = 0°$) compared to a tilted configuration ($\theta = 5°$). The reflected wave height, normalised by the diameter of the bar b, was monitored by using the maximum height achieved by the flow (γ_L=0.5) at the end wall. A typical evolution of the wave height for different tilted angle was illustrated in Fig. 6. The molten free surface height continued to increase at

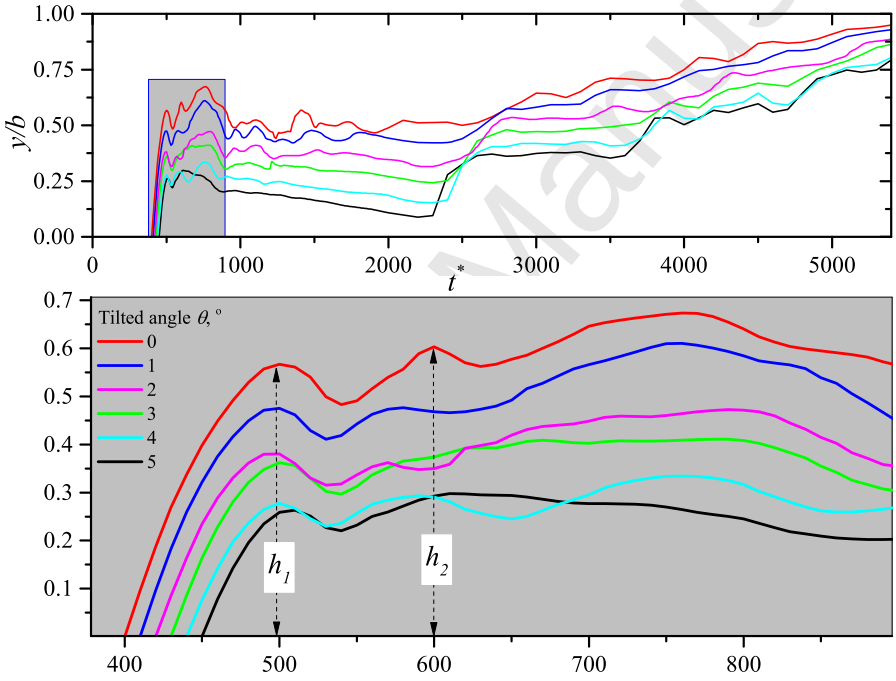

Figure 6: Reflected wave height *v.s.* simulation time t for different tilted angle θ at $Re = 16,700$. The terms h_1 and h_2 represent the primary and the secondary reflected wave heights.

the beginning and subsequently dropped due to the primary reflect wave break up (h_1). The increasing trend of the free surface was observed to resume, up to a point where another reflected wave break up occurred, known to be the secondary reflected wave break up h_2. This kind of trend was seen to be recurring until the backward travelling flow and the mainstream flow was reunited. Furthermore, correlations between the normalised primary and secondary reflected

wave height have been established for various θ and Re defined in this work, shown in Fig. 7. The results showed that the reflected wave height, for both h_1

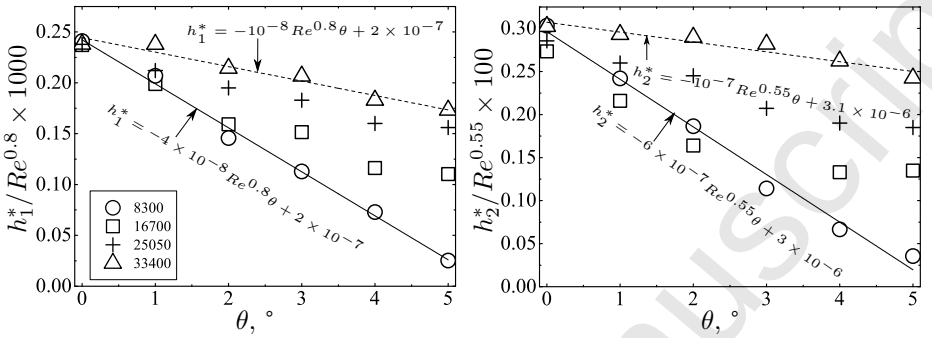

Figure 7: Normalised primary (left) and secondary (right) reflected wave heights correlations at various θ and Re.

and h_2, decreased with increasing titled angle. For h_1 and h_2, they followed the trends of $Re^{0.8}$ and $Re^{0.55}$, respectively.

The next step was to investigate the severity of the free surface fluctuations generated by the ongoing reflected wave break-ups that made contact with the incoming main stream flow. This analysis was performed by evaluating cross-sectional free surface fluctuation in the casting cavity. Following the work of Hibbeler and Thomas (2010) and Li et al. (2017), the free surface fluctuation was represented by a defined variable Δy:

$$\Delta y = y_{max} - y_{min}, \tag{20}$$

where y_{max} and y_{min} were the maximum and minimum $y-$coordinates of the cross-sectional free surface. The free surface fluctuation computation was carried out at $z/a = 0.9$ as this location was situated in the vicinity of the wave break-ups. A typical evolution of Δy was depicted in Fig. 8 and it demonstrated that the severity of free surface fluctuation relied heavily on the reflected wave break-ups. Furthermore, the intensity of the free surface fluctuation demonstrated the importance of θ in suppressing these wave break-ups.

The standard deviation from the primary wave break-up up to the secondary wave break-up was further computed for different θ and correlations were es-

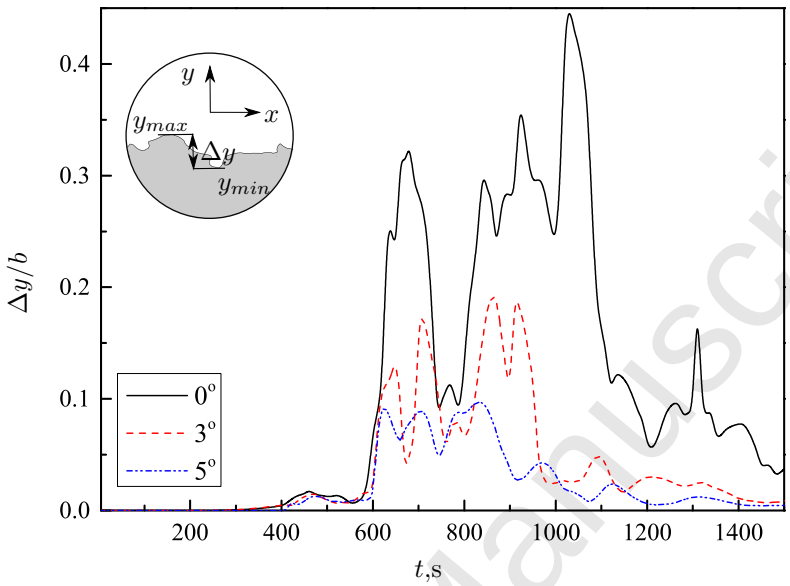

Figure 8: Variation of Δy normalised by bar diameter b against filling time t at xy plane where $z/a = 0.9$ for $\theta = 0°$ (black solid line), 3° (red dashed line) and 5° (blue dashed dotted line), respectively.

tablished for various Re, as illustrated in Fig. 9. The correlations were fitted using power law functions. The trend was observed to be shifting consistently with increasing Re but differs significantly for the highest Re. As expected, minimal free surface fluctuation was identified when Re was low, leading to a low standard deviation in the alloy free surface. In contrast, for highest Re, the standard deviation was expected to be high due to fast flowing alloy resulting in the occurrence of sloshing effects between front and end walls.

3.2. Unfilled air cavity

The filling process was extended with the aim to fill the whole casting cavity perfectly in a single attempt to reduce unwanted alloy wastage in both risers. Furthermore, no air void should be present in the casting cavity when completely filled. In this current work, the presence of air void in the casting cavity, known as air cavity (ε_A), was evaluated as the ratio of volume of air over the total volume of the casting cavity. Typical ε_A behaviour for various θ across the

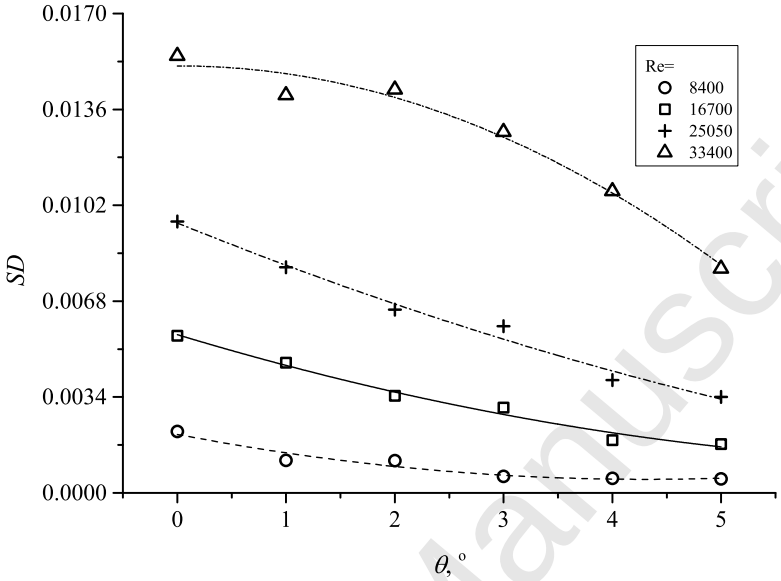

Figure 9: Standard deviation from the primary to the secondary wave break-up across various θ for at different Re presented as markers. The established correlations are expressed as lines.

filling duration for a fixed Re was illustrated in Fig. 10. The air cavity was expected to be full ($\varepsilon_A = 1$) initially as molten alloy had yet to enter the casting cavity. The air cavity ε_A subsequently reduced with increasing filling time. The decreasing trend was observed to be approximately linear. As expected, the slope increased with increasing Re, leading to a shorter filling duration. The air

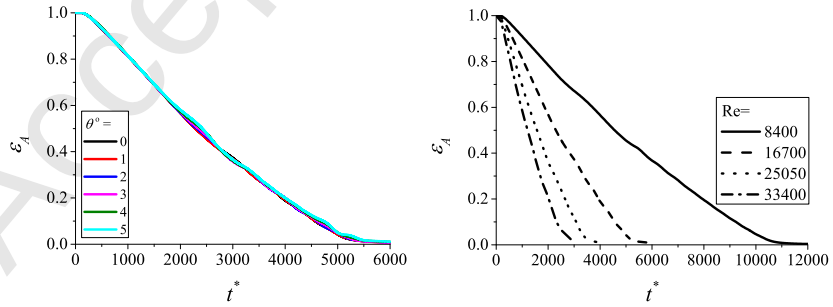

Figure 10: Typical evolution of air cavity for various θ at $Re = 16,700$ (left) and various Re at $\theta = 0$ (right).

cavity for each θ was evaluated and correlations were established for different

313 *Re*. The evaluated values were selected based on the filling time, where the rate
314 of change of air cavity over time period of 0.01 s was less than 1% for the worst
315 configuration, which was thought to be $\theta = 5°$. The correlations were depicted in Fig. 11. The air cavity was observed to increase systematically with increasing

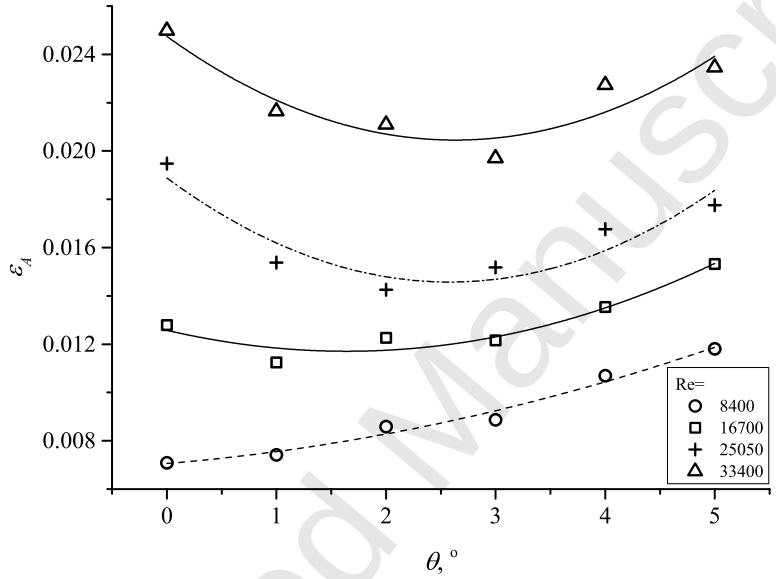

Figure 11: Relationship of air cavity across various θ for at different *Re* presented as markers. The established correlations are expressed as lines.

316

317 θ when *Re* was low. Regardless of the tilted angle, the overall air cavity was
318 expected to increase with increasing *Re*, revealing a high risk in the occurrence
319 of large air void, hence leading to an increase in ε_A. Furthermore, the air cavity
320 at $\theta = 0°$ increased dramatically, overtaking the air cavity at $\theta = 5°$.

321 *3.3. Identification region for good quality cast*

322 In this section, Figs. 9 (free surface fluctuation) and 11 (air cavity) were
323 utilised in attempting to identify the best possible uphill filling configuration
324 to produce good quality cast. Scaling of the fitted expressions was performed
325 for each parameter and the final results were illustrated in Fig. 12. The free
326 surface fluctuation fitted parameter was scaled by $Re^{1.4}$ and the air cavity fitted
327 expressions were scaled by $Re^{0.91}$. It was observed that the free surface fluctu-

ation had a similar trend, whereby the free surface fluctuation decreased with increasing θ and the effect worsened with increasing Re. In contrast, the air cavity had a similar trend, as discussed in the previous section. They behaved in a near linear fashion at low Re, and with increasing Re started to alter the trend gradually towards a quadratic trend. After further analysis, the region that has the potential to produce good quality cast internally and externally was identified and highlighted in Fig. 12. The region of operation was identified to be between 2° and 3°, providing a good balance between low free surface fluctuation and air cavity. It can be observed that although the air cavity was low for θ lower than 2°, the free surface fluctuation were observed to be high. The effect was observed to be vice-versa when θ was larger than 4°. The highlighted region could be used as a guideline for manufacturers designing bar-like casts. The first step for the manufacturers were to determine a desire θ for the configuration. The subsequent step was then to decide on a Re in which the standard deviation of free surface fluctuation and air cavity evaluation could be conducted. Although an obvious choice would be a low Re, care should be taken as this would significantly decrease the production rate of the cast.

4. Conclusions

The current work aimed to investigate the possibility of utilising an uphill filling system in a Co-Cr-W alloy bar-shape casting and to identify an optimised uphill filling configuration for the type of mould design. The main findings were summarised as follows:

1. A design mould of small dimensions with a tilted angle reduced the free surface fluctuation. These fluctuations were mainly caused by the reflected wave break-ups at the end wall. Findings indicated that this type of filling system has the potential to improve the casting quality.
2. The existence of tilted angle θ reduced the height of the reflected wave: The primary and secondary wave heights was reduced by 54% and 51%,

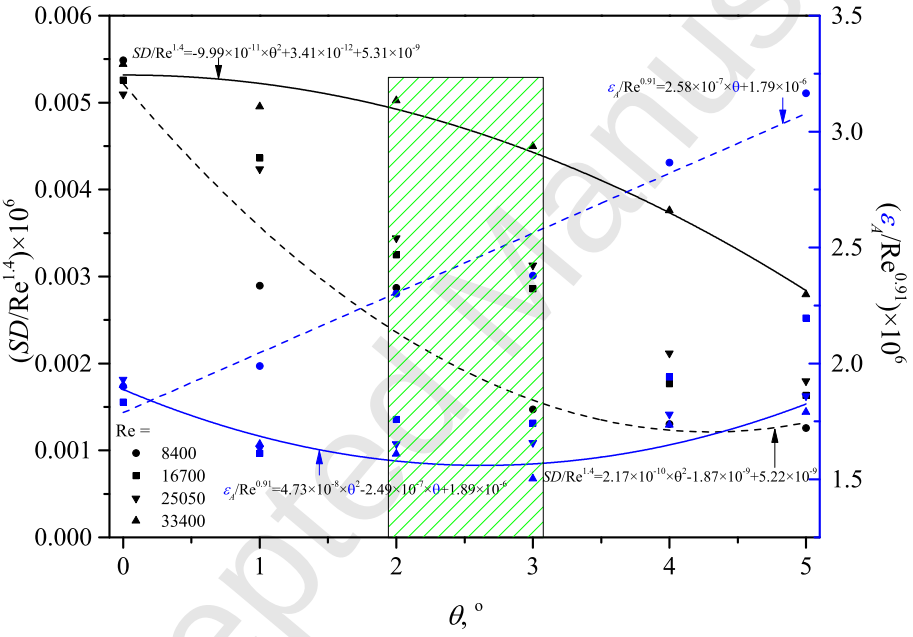

Figure 12: Scaled standard deviation of free surface fluctuation computed from the primary to the secondary wave break-up across various θ for at different Re presented in black. Scaled air cavity across various θ for at different Re presented in blue. Highlighted region represents suitable θ that produce good quality cast.

respectively. On the other hand, the free surface fluctuations were reduced by 49% when θ was increased from 0° to 5°.

3. The existence of air cavity ϵ_A was observed to accumulate in the region of the highest part of the bar (near end wall) at the end of the filling process. Furthermore, ϵ_A was found to be increased with increasing θ. The computed air cavity volume was found to increase 40% with increasing θ from 0° to 5°.
4. An optimised region was identified when the a diagram was generated which consist of a balance between 2° and 3° . The free surface fluctuation was observed to decrease with increasing θ and the trends were scaled by $Re^{1.4}$. The air cavity was observed to be a near linear trend at low Re and gradually evolved into a quadratic trend with increasing Re. This trend was scaled by $Re^{0.91}$. An optimised range of tilting angle (2° to 3°) was proposed as a compromise to reduce the free surface fluctuations and maintain a perfect shape of the casting at the end of the filling stage.

Acknowledgements

The authors acknowledge the European Regional Development Fund (ERDF) through the Welsh Government financial contribution to undertake this study under the ASTUTE 2020 operation. The contribution by Dr. J. Cherry and Dr. H.M. Davies in conducting the experiments is also appreciated. Additionally, the authors would like to thank Professor John Campbell for his fruitful discussion and the reviewers for their work, which has contributed to this paper.

References

Ramshaw J. D. and Trapp J. A., 1976. A numerical technique for low-speed homogeneous two-phase flow with sharp interfaces. Journal of Computational Physics 21(4), 438-453.

Hirt C. W. and Nichols W.S., 1981. Volume of fluid (VoF) method for the dynamics of free boundaries. Journal of Computational Physics 39(1), 201-225

Chan K.S., Pericleous K., Cross M., 1991. Numerical simulation of flows encountered during mold-filling. Appl. Math. Modelling. 15, 625-631.

Ravindran K., Lewis R.W., 1998. Finite element modelling of solidification effects in mould filling. Finite Elements in Analysis and Design. 31, 99-116.

Kim K.D., Yang D.Y., Jeong J.H., 2006. Adaptive refinement techniques based on tetrahedral and hexahedral grids for finite element analysis of mold filling in casting processes. Comput. Methods Appl. Mech. Engrg. 195, pp 6799-6281.

Pang S., Chen L., Zhang M., Yin Y., Chen T., Zhou J., Liao D., 2010. Numerical simulation two phase flows of casting filling process using SOLA partical level set method. Appl. Math. Modelling. 34, 4106-4122.

Mirbagheri S.M., Esmaeileian H., Serajzadeh S., Varahram N., Davami P., 2003. Simulation of melt flow in coated mould cavity in the casting process. Journal of Materials Processing Technology. 142, 495-507.

Zhang L., Belblidia F., Davies M. H., Lavery P. N., Brown G.R.S., Davies D., 2017. Optimizing gate location to reduce metal wastage: CoCrW alloy filling simulation. Journal of Materials Processing Technology. 240, 249-254.

Sun Z., Hu H., Chen X., 2008. Numerical optimization of gating system parameters for a magnesium alloy casting with multiple performance characteristics. Journal of Materials Processing Technology. 199, 256-264.

Kermanpur A., Mahmoudi S., Hajipour A., 2008. Numerical simulation of metal flow and solidification in the mult-cavity casting moulds of automotive components. Journal of Materials Processing Technology, 206, 62-68.

Du J., Chong X., Jiang Y., Feng J., 2015. Numerical simulation of mold filling process for high chromium cast iron matrix composite reinforced by ZTA

ceramic particles. International Journal of Heat and Mass Transfer. 89, 872-833.

Assar A.M., 1999. The structure and soundness of Al-4.5Cu ingots cast in open mould using different filling rate. Journal of Materials Processing Technology. 86, 146-151.

Cox M., Wickins M., Kuang J.P., Harding R.A., Campbell J., 2000. Effect of top and bottom filling on reliability of investment castings in Al, Fe, and Ni based alloys. Materials Science and Technology. 16, 1445-1452.

Liu S., Cao F., Zhao X. Jia Y., Ning Z. and Sun J., 2015. Characteristics of mold filling and entrainment of oxide film in low pressure casting of A356 alloy. Materials Science & Engineering A. 626, 159-164.

Campbell J., 1991. Castings; Butterworth-Heinemann Ltd, Linacre House, Jordan Hill, Oxford, UK, OX2 8DP.

Carswell D., Davies M.H., Lavery P.N., James J., Brown G.R.S., Fourlaris G., 2011. Simulation for mould design of a gravity sand casting (final report). Unpublished internal report. ASTUTE Project Office contact: Tel. +44 1792 606378, Email: info@astutewales.com.

Valencia J. J. and Quested P. N., Thermophysical Properties, ASM Handbook vol. 15 Casting, 468-481.

Brackbill J.U., Kothe D.B., Zemach C., 1991. A continuum method for modeling surface tension. Journal of Computational Physics. 100, 335-354.

Stefanescu D.M., Upadhya G., Bandyopadhyay D., 1990. Heat transfer-solidification kinetics modeling of solidification of castings. Metallurgical Transactions A 21 (3), 997-1005.

Xie F., Zheng X., Triantafyllou S.S., Constantiides Y., Zheng Y. and Karniadakis G. E., 2017. Direct numerical simulations of two-phase flow in a inclined pipe. J. Fluid Mech. 825, 189-207.

Li Z., Wang E., Zhang L., Xu Y., Deng A., 2017. Influence of vertical electromagnetic brake on the steel/slag interface behaviour in a slab mold. Metallurgical and Materials Transactions B. 48B, 2380-2402.

Hibbeler C.L., Thomas B.G., 2010. Investigation of mold flux entrainment in CC molds due to shear layer instability. Assoc. Iron Steel Technology, Warrendale, PA, CCC Report 201001, Aug.12.